Research Article

Journal of Environmental Nanotechnology

Sustainable W–$BiVO_4$ Nanocatalysts for Visible-light Removal of Reactive Black 5: Physicochemical Characterization and Multiresponse Optimization

R. Ramani[1], P. Maniraj[2*], R. Aruna[3], S. Santhakumari[4], Sunder Rajan Sundaram Mariappan[5] and G. Chandrasekaran[6]

[1]Department of Electrical and Electronics Engineering, Dr M.G.R Educational and Research Institute, Chennai, TN, India
[2]Department of Electrical and Electronics Engineering, M. Kumarasamy College of Engineering, Thalavapalayam, Karur, TN, India
[3]Department of Mechanical Engineering, Rajalakshmi Engineering College, Chennai, TN, India
[4]Department of Physics, Shrimati Indira Gandhi College, Tiruchirappalli, TN, India
[5]Department of Mechanical Engineering, Francis Xavier Engineering College, Tirunelveli, TN, India
[6]Department of Mechanical Engineering, Lord Jegannath College of Engineering and Technology, Nagercoil, TN, India
Received: 28.07.2026 Accepted: 27.08.2026 Published: xx.xx.xxxx
*manirajperumal86@gmail.com

ABSTRACT

This study reports the green synthesis of pristine $BiVO_4$ and tungsten-doped $BiVO_4$ (W–$BiVO_4$) nanocatalysts using dragon-fruit-peel extract for the visible-light degradation of Reactive Black 5 (RB5). The novelty lies in integrating waste-derived green synthesis, multiresponse statistical optimization, machine-learning prediction, and kinetic evaluation within a single RB5-treatment framework. The W–$BiVO_4$ nanoparticles exhibited irregular rod-like and ellipsoidal morphologies with a mean particle size of 48.6 ± 10.4 nm. SEM–EDX confirmed the presence of Bi, V, O, and W, although this analysis alone does not conclusively establish substitutional incorporation of W into the $BiVO_4$ lattice. The synthesized $BiVO_4$ exhibited an estimated optical band gap of 2.55 eV, supporting visible-light activation. The photocatalytic performance of W–$BiVO_4$ was investigated using a 29-run Box–Behnken design by varying initial RB5 concentration, catalyst dosage, initial pH, and W-doping level. The highest experimental performance was 93.40% RB5 removal with an apparent pseudo-first-order rate constant of 0.01947 min^{-1} at 20 mg L^{-1} RB5, 1.20 g L^{-1} catalyst dosage, pH 6, and 3 wt.% W doping. The quadratic RSM models were statistically significant and achieved R^2 values of 0.9991 for RB5 removal efficiency and 0.9831 for the apparent pseudo-first-order rate constant. Multiresponse optimization predicted 93.51% RB5 removal and an apparent pseudo-first-order rate constant of 0.02003 min^{-1} at an initial RB5 concentration of 20.68 mg L^{-1}, W–$BiVO_4$ dosage of 1.162 g L^{-1}, initial pH of 5.30, and W-doping level of 3.44 wt.%, with an overall desirability of 1.000. Among six machine-learning models evaluated using leave-one-out cross-validation, Gaussian process regression provided the best prediction of RB5 removal efficiency (R^2 = 0.991), whereas support vector regression provided the best prediction of the apparent pseudo-first-order rate constant (R^2 = 0.924). These findings demonstrate the potential of combining green W–$BiVO_4$ synthesis, experimental optimization, and machine-learning prediction for visible-light treatment of RB5-containing wastewater.

Keywords: Reactive black 5; Adsorption; Machine learning; Phytotoxicity; Green synthesis.

1. INTRODUCTION

The persistent release of dye-contaminated wastewater from textile, printing, leather, paper, and pharmaceutical industries has emerged as an environmental concern worldwide. Their accumulation reduces light penetration, inhibits photosynthetic activity, and generates toxic and carcinogenic intermediates that threaten aquatic organisms and health. As a result, considerable research has focused on developing efficient, sustainable, and environmentally benign technologies for the removal of persistent pollutants. In photocatalytic dye treatment, decolorization or removal reflects a decrease in the parent dye concentration or visible absorbance, whereas degradation involves chemical transformation of the dye molecule. Complete mineralization further requires conversion toward inorganic products such as CO_2, H_2O, and mineral ions. Therefore, removal efficiency alone does not establish complete degradation or mineralization, and identification of intermediates or TOC/COD analysis is required for definitive confirmation. Among visible-light photocatalysts, $BiVO_4$ has attracted considerable interest because of its narrow band gap (~2.4 eV), low toxicity, and favorable electronic properties. However, rapid charge-carrier recombination and poor charge transport limit its photocatalytic efficiency.

Among these approaches, tungsten (W) doping has proven particularly effective in improving the electronic properties of $BiVO_4$ by introducing oxygen

vacancies, enhancing charge separation, and facilitating visible-light absorption. Mechanistically, W^{6+} can substitute for V^{5+} sites in the $BiVO_4$ lattice and introduce shallow donor states near the conduction band, thereby increasing electron density and electrical conductivity. This modification can facilitate photogenerated-electron transport and reduce electron–hole recombination. W incorporation can also alter the defect chemistry and oxygen-vacancy population, which may provide additional surface-active sites and influence charge-transfer behaviour. However, oxygen vacancies are not universally beneficial because excessive bulk vacancies can also act as recombination centers; therefore, their effect depends on concentration and location. W-doped $BiVO_4$ containing oxygen vacancies supported on reduced graphene oxide exhibited a ciprofloxacin degradation rate constant more than ten times greater than pristine $BiVO_4$ under UV irradiation, demonstrating the synergetic contribution of tungsten doping, oxygen vacancies, and conductive carbon supports (Zhao *et al.* 2021). Likewise, a W-$BiVO_4$/$Cs_2AgBiBr_6$ S-scheme heterojunction achieved over 92% degradation of both ofloxacin and meloxicam within only 40 min under visible light, highlighting the remarkable potential of tungsten-modified $BiVO_4$ photocatalysts for pharmaceutical wastewater treatment (Liu *et al.* 2025). Furthermore, green hydrothermally synthesized W- and Mo-doped $BiVO_4$ nanoparticles exhibited a single monoclinic crystal structure with abundant oxygen vacancies and significantly enhanced Rhodamine B degradation compared with pristine $BiVO_4$, confirming the effectiveness of transition-metal doping in improving photocatalytic efficiency (Tsay *et al.* 2023). Although W-doped $BiVO_4$ has demonstrated improved photocatalytic performance, most reported studies focus on conventional synthesis routes, pharmaceutical or model-dye degradation, and single-response photocatalytic evaluation. Notably, fruit-peel-mediated green routes have already been used to prepare tungsten-oxide photocatalysts; for instance, WO_3 nanoparticles were green-synthesized using *Selenicereus undatus* (dragon-fruit) peel extract, yielding a monoclinic structure with an indirect band gap of about 2.23 eV (Auxilia Ruby *et al.* 2025). Limited information is available on dragon-fruit-peel-assisted W-doped $BiVO_4$ for Reactive Black 5 treatment, particularly when removal efficiency and kinetic response are optimized simultaneously and linked with machine-learning prediction and phytotoxicity assessment.

Plant-mediated synthesis has been increasingly applied to semiconductor photocatalysts because phytochemical-rich extracts can assist precursor complexation, nucleation, particle stabilization, and surface functionalization. However, comparatively limited attention has been given to plant-assisted W-doped $BiVO_4$ systems integrated with photocatalytic optimization, predictive modelling, and post-treatment phytotoxicity evaluation (Yan *et al.* 2018). Similar green synthesis strategies have successfully produced highly active photocatalysts. For example, zeolite-supported CeO_2@PBI composites containing green-synthesized ceria achieved approximately 98% Reactive Black 5 degradation under UV irradiation (Zaharieva *et al.* 2026). Green-synthesized NiO nanoparticles prepared using *Fioria vitifolia* extract exhibited 88.9% RB5 degradation under visible light while simultaneously demonstrating antibacterial, antioxidant, and anticancer activities (Dash *et al.* 2026). Likewise, Er-doped ZnO nanoparticles derived by Mangifera indica gum achieved nearly complete MB degradation together with excellent photocatalyst reusability (Silva *et al.* 2024). Similarly, green-synthesized TiO_2 nanocomposites prepared using *Moringa oleifera* leaf extract achieved efficient photocatalytic degradation of methylene blue under solar irradiation while exhibiting multifunctional biological activity (Anishia *et al.* 2025). These studies clearly demonstrate that plant-mediated synthesis offers an environmentally benign route for developing efficient multifunctional photocatalysts.

Recent investigations have also noted the significance of evaluating the environmental safety of photocatalytic materials and their degradation products. Bi_2MoO_6/N-doped carbon nanofiber membranes achieved 97% tetracycline degradation while exhibiting excellent reusability and no phytotoxic effects on Vigna radiata seeds (Xue *et al.* 2022). Similarly, $Bi_2VO_{5.5}$ photocatalysts demonstrated efficient photocatalytic and piezo-photocatalytic degradation of MB together with favorable phytotoxicity characteristics (Kumar *et al.* 2022). Biological degradation of Reactive Black 5 using Acinetobacter baumannii JC359 achieved nearly complete dye decolorization under optimized Box-Behnken Design conditions, while phytotoxicity analysis confirmed the environmental safety of the degradation products (Ameenudeen *et al.* 2021). In addition, green-synthesized Fe_3O_4 nanoparticles mediated by Albizia lucidior exhibited photocatalytic dye degradation together with antioxidant properties and promoted the growth of Vigna radiata seedlings (Hadkar *et al.* 2025). These findings indicate that ecotoxicity evaluation should accompany photocatalytic performance studies to ensure sustainable wastewater treatment technologies. Photocatalytic disappearance of the parent dye does not necessarily demonstrate environmental safety because partially transformed intermediates may remain biologically active or toxic. Therefore, Vigna radiata seed germination and early-growth responses provide a complementary biological endpoint for comparing untreated and photocatalytically treated RB5 solutions. This assessment helps determine whether reduced dye concentration is accompanied by reduced phytotoxicity, although it does not substitute for comprehensive aquatic ecotoxicity or chemical-intermediate analysis

RSM and machine learning address different but complementary aspects of photocatalytic process

analysis. RSM provides interpretable quadratic relationships, factor effects, and interactions within the experimental design space. Mult response optimization identifies operating conditions that balance both RB5 removal efficiency and the apparent pseudo-first-order rate constant rather than optimizing either response independently. Machine-learning models provide an additional data-driven assessment of nonlinear predictive relationships. Their combined use therefore enables statistical interpretation, simultaneous response optimization, and comparative predictive validation within a unified framework.

The novelty of this study lies in integrating dragon-fruit-peel-assisted green synthesis of W-doped $BiVO_4$ with visible-light photocatalytic degradation of Reactive Black 5 (RB5), multi-response RSM optimization, machine-learning-based prediction, and post-treatment phytotoxicity assessment. A four-factor Box–Behnken design was employed to simultaneously optimize RB5 removal efficiency and the apparent pseudo-first-order rate constant, thereby linking treatment efficiency with degradation kinetics. Six complementary machine-learning algorithms, RF, MLP–ANN, GPR, KNN, XGBoost, and SVR, were comparatively evaluated using leave-one-out cross-validation to assess predictive performance under the limited experimental dataset. In addition, *Vigna radiata* phytotoxicity testing provided a preliminary assessment of the environmental compatibility of the treated solution. Thus, the study establishes an integrated material–process–prediction–safety framework for sustainable visible-light treatment of RB5-contaminated wastewater.

2. MATERIALS AND METHODOLOGY

2.1 Preparation of the Dragon Fruit Peel Extract

Fresh dragon-fruit (*Hylocereus polyrhizus*) peels were washed with water to remove adhering impurities. The peels were shade-dried under ambient conditions and subsequently oven-dried at 60 °C for 24 h before being ground into a fine powder. 20 g of the powder was mixed with 200 mL of distilled water and heated at 80 °C for 30 min under continuous stirring (Kistan *et al.* 2025). The mixture was cooled and filtered. The obtained extract was stored at room temperature and used for the fabrication of the composite.

2.2 Green Synthesis of the $BiVO_4$ NPs

Figure 1 illustrates the biosynthesis process of $BiVO_4$ nanoparticles ($BiVO_4$-NPs) using dragon fruit peel extract as a green reducing and stabilizing agent.

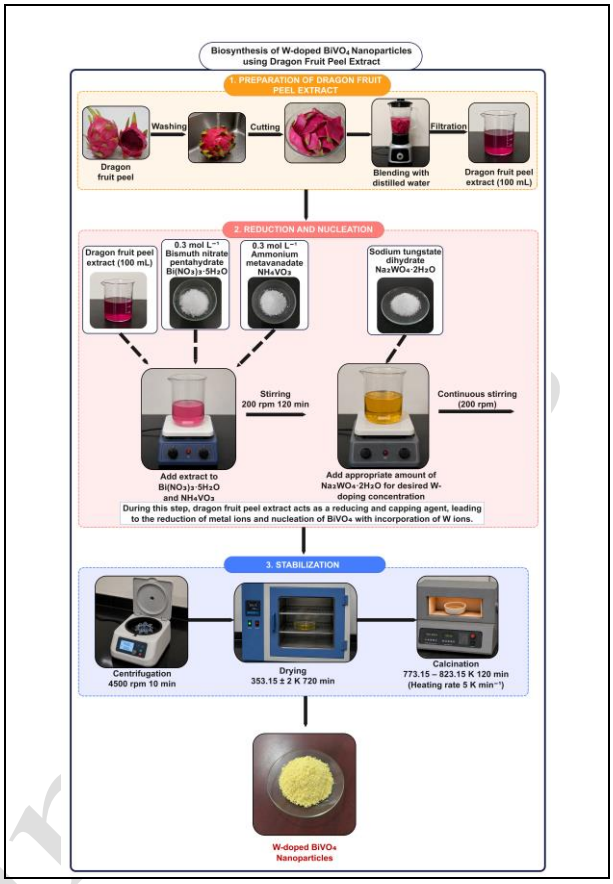

Fig. 1: Biosynthesis of $BiVO_4$-NPs using dragon fruit peel extract with bismuth nitrate pentahydrate and ammonium metavanadate as precursor materials

Equal volumes of 100 mL of 0.3 mol L^{-1} $Bi(NO_3)_3 \cdot 5H_2O$ and 100 mL of 0.3 mol L^{-1} NH_4VO_3 were prepared using 14.55 and 3.51 g of the respective precursors. Each solution contained 0.030 mol of precursor, thereby providing a Bi: V molar ratio of 1:1. Dragon-fruit-peel extract (100 mL) was subsequently added, and the mixture was stirred at 200 rpm for 120 min.

The nominal W-doping level was expressed as the mass percentage of elemental W relative to the final W-$BiVO_4$ catalyst:

$$W(\text{wt.}\%) = \frac{m_W}{m_{BiVO_4} + m_W} \times 100 \qquad \ldots (1)$$

The required $Na_2WO_4 \cdot 2H_2O$ mass was calculated as:

$$m_{Na_2WO_4 \cdot 2H_2O} = \frac{w}{100 - w} m_{BiVO_4} \left(\frac{329.85}{183.84}\right), \ldots (2)$$

where w is the required nominal W content (1, 3, or 5 wt.%), 329.85 g mol^{-1} is the molar mass of $Na_2WO_4 \cdot 2H_2O$, and 183.84 g mol^{-1} is the atomic mass of W. The stated doping values therefore represent

nominal elemental-W contents rather than sodium-tungstate concentrations.

Subsequently, an appropriate amount of sodium tungstate dihydrate ($Na_2WO_4 \cdot 2H_2O$) was added to obtain the desired tungsten doping concentration, and the reaction mixture was stirred to ensure homogeneous addition of W ions into the $BiVO_4$ lattice (Pramila *et al.* 2024). The resulting suspension was centrifuged at 4500 rpm for 10 min, and the recovered solid was dried at 80 ± 3 °C for 12 h. The dried material was subsequently calcined at 500–550 °C for 2 h using a heating rate of 5 °C min^{-1}.

2.3 Characterization of Dragon Fruit Peel Extract

The phytochemical constituents of the peel extract were analyzed by high-performance liquid chromatography. The analysis was done with a C18 reverse-phase column (3.9 × 150 mm, 4 µm) coupled to a Lab Solutions data acquisition and processing system. A gradient elution program was employed using two phases: (1) water consisting of 0.3% formic acid and (B) methanol consisting of 0.03% formic acid. The chromatographic separation was conducted at a flow rate of 1.0 mL/min at 280 nm. The injection volume was fixed at 20 µL, while the column was maintained at room temperature (298 ± 2 K). The retention time and concentration of the detected phytochemical compounds were determined from the resulting chromatograms. Phytochemicals were identified by comparing their retention times with those of analytical-grade standards of gallic acid, catechin, chlorogenic acid, caffeic acid, ferulic acid, rutin, quercetin, kaempferol, betanin, phyllocactin, and isorhamnetin. External calibration curves were prepared at five concentration levels within 0.1–10 µg mL^{-1} and analyzed in triplicate. Quantification was performed from the corresponding peak-area calibration equations. The limits of detection and quantification were calculated as 3.3σ/S and 10σ/S, respectively, where σ is the standard deviation of the response and S is the calibration-curve slope. The identified compounds, retention times, peak areas, and concentrations are presented in Table 3.

2.4 Characterizations of $BiVO_4$ -NPs

The crystalline phases were examined by X-ray diffraction using Cu Kα radiation with a wavelength of 1.5406 Å. Patterns were recorded over 2θ=10–80∘ at 40 kV and 40 mA, using a step size of 0.02° and a scan rate of 2° min^{-1}. In addition, the average crystallite size (dc) and interplanar spacing (d) were determined using Eqs. (1) and (2), correspondingly (Kistan *et al.* 2026).

$$d_c = \frac{0.94^* \lambda_{Cu-\alpha}}{\beta^* \cos(\theta)} \quad \ldots (3)$$

$$d = \frac{\lambda_{Cu-\alpha}}{2^* \text{sen}(\theta)} \quad \ldots (4)$$

Whereas β denotes total width at half maximum (FWHM); and θ indicates Bragg diffraction angle (◦).

The functional phases present in the synthesized specimen were examined using FTIR with a PerkinElmer Spectrum Frontier spectrometer with a range of 4000–400 cm^{-1}. Morphological analysis was performed using a Field Emission Scanning Electron Microscope (FESEM-ZEISS), and particle size analysis was done using ImageJ software (Kistan *et al.* 2024). The elemental composition of the synthesized samples was examined by SEM equipped with an EDS system. The textural characteristics, including pore volume, specific surface area, and pore size distribution, were evaluated through N_2 adsorption–desorption analysis using a Micromeritics ASAP 2020 Plus analyzer. Before analysis, approximately 0.20 g of each sample was degassed under vacuum at 120 °C for 6 h to remove physically adsorbed moisture and gases. After cooling under vacuum, N_2 adsorption–desorption measurements were conducted at 77 K. The BJH method was used to estimate pore size and pore volume from adsorption data collected over a relative pressure (P/P_0) range of 0–1, and the BET method was employed to determine the specific surface area (Sajid *et al.* 2024). The zeta potential (ZP) of the synthesized nanoparticles was measured using a Malvern Zetasizer Nano ZS (ZEN3600, UK). The point of zero charge (pHZPC) was determined using the 11-point pH drift method. Thermal stability was evaluated by thermogravimetric analysis (TGA) and derivative thermogravimetry (DTG) through a Shimadzu TGA-60/60H analyzer. Measurements were conducted under an artificial air atmosphere at 100 mL min^{-1} over 299.15–1274.15 K at 10 K/min. Optical properties were investigated using a UV–Vis spectrophotometer fitted with a DRA-CA-301 Labsphere diffuse reflectance accessory. Diffuse-reflectance spectra were recorded over 200–800 nm, and the optical band gap was determined using the Tauc relation combined with the Kubelka–Munk function, F(R)=(1−R)2/(2R), as expressed in Eqs. (3)–(5),(Nalina *et al.* 2026).

$$F(R) = \frac{(1-R_\infty)^2}{2R_\infty} \quad \ldots (5)$$

$$h\nu = \frac{1240}{\lambda} \quad \ldots (6)$$

$$R = \frac{1}{A} \quad \ldots (7)$$

here $h\nu$ denotes incidental photon energy (eV), $R\infty$ denotes diffuse reflectance, and $F(R)$ indicates Kubelka–Munk function; λ represents the wavelength corresponding to the maximum absorption (nm),. The exponent n depends on the nature of the electronic transition, with $n = 0.5$ for direct transitions and $n = 2$ for indirect transitions. Monoclinic $BiVO_4$ was treated as an

indirect allowed band-gap semiconductor; therefore, n=2 was used in the adopted Tauc expression. The linear region of the [F(R)hν]1/2 versus hν plot was extrapolated to the energy axis to estimate the indirect optical band gap.

2.5 Experimental Design and Response Measurement

Photocatalytic degradation of RB5 through W-doped $BiVO_4$ was investigated using a four-factor, three-level Box–Behnken design (BBD). The RB5 concentration, catalyst dosage, initial pH, and W-doping level were selected as independent variables (Salari *et al.* 2022). RB5 removal efficiency and the pseudo-first-order constant were considered the responses. Design-Expert generated 29 experimental runs, including five centre-point repetitions for estimating pure error. Pure error was estimated from the variation among the five replicated centre-point measurements, providing four degrees of freedom. The residual sum of squares was partitioned into pure-error and lack-of-fit components. Lack of fit was evaluated by comparing its mean square with the pure-error mean square using an F-test at α=0.05. The 24 non-centre-point combinations were conducted once, while the centre condition was independently repeated five times. Thus, the design contained 29 total runs, and experimental error was estimated from the five centre-point replicates rather than from complete replication of all design combinations.

Table 1. Factors and levels used in the BBD

Factor	Variable	Unit	−1	0	+1
A	RB5 concentration	mg/L	20	40	60
B	Catalyst dosage	g/L	0.40	0.80	1.20
C	Initial pH	–	3	6	9
D	W doping	wt.%	1	3	5

Removal efficiency was evaluated using eqn (6):

$$R(\%) = \frac{C_0 - C_t}{C_0} \times 100 \quad \ldots (8)$$

whereas C_0 and C_t shows the initial and final concentrations after irradiation time t, respectively. The apparent rate constant was calculated from the pseudo-first-order kinetic equation (7):

$$\ln\left(\frac{C_0}{C_t}\right) = kt \quad \ldots (9)$$

whereas k denotes the apparent rate constant in min

2.6 Response-surface Modelling and Optimization

The experimental responses were fitted to a Second-order polynomial model:

$$Y = \beta_0 + \sum_{i=1}^{4} \beta_i X_i + \sum_{i=1}^{4} \beta_{ii} X_i^2 + \sum_{i<j}^{4} \beta_{ij} X_i X_j \ldots (10)$$

Here, Y is the predicted response, X_i and X_j are coded independent variables (process parameters), β_0 is the intercept (constant term), β_i shows linear coefficients, β_{ii} shows quadratic coefficients that account for curvature of the response surface, and β_{ij} shows interaction coefficients describing the combined effect of two independent variables on the response. This second-order regression model is widely employed in Response Surface Methodology (RSM) to establish relationships among input variables and response, enabling prediction of response and identification of the optimum operating conditions.

Analysis of variance was used to assess model importance and factor effects. Terms with $p < 0.05$ were measured as numerically important. Model adequacy was evaluated using the coefficient of determination, adjusted and predicted R^2, coefficient of variation, adequate precision, lack of fit, and residual diagnostic plots. Contour and 3D response-surface graphs were created to illustrate factor interactions.

Simultaneous optimization was performed using the desirability-function method. The four factors were maintained within their investigated ranges, while RB5 removal and the rate constant were maximized. The combined desirability was expressed as:

$$D = (d_1 d_2 \cdots d_m)^{1/m} \quad \ldots (11)$$

where d_i is the desirability of each response and m is the number of responses.

2.7 Photocatalytic Tests

Reactive Black 5 was selected as the target pollutant, while W–$BiVO_4$ containing nominal W-doping levels of 1, 3, and 5 wt.% was employed as the photocatalyst in the Box–Behnken experiments. Pristine $BiVO_4$ was tested separately as the undoped reference catalyst. Photocatalytic experiments were conducted in a 250 mL cylindrical borosilicate batch reactor containing 100 mL of RB5 solution. A 300 W xenon lamp equipped with a 420 nm cut-off filter provided visible light over approximately 420–780 nm. The lamp was positioned 15 cm from the reactor, and the incident intensity at the solution surface was maintained at 100 mW cm^{-2}. The photocatalytic experiments were conducted in two stages: (i) an initial dark adsorption period of 60 min without light irradiation to establish adsorption–desorption equilibrium, followed by (ii) visible-light irradiation for the photocatalytic decomposition process. During the irradiation stage, aliquots were collected at predetermined intervals between 0 and 180 min, filtered

through a 0.45 µm membrane, and diluted at a ratio of 1:10 (v/v) (Ma and Lin, 2021). The 1:10 dilution-maintained sample absorbance within the linear RB5 calibration range of 0–10 mg L^{-1} and prevented detector saturation. The concentration obtained from the calibration curve was multiplied by the dilution factor of 10 when calculating the residual RB5 concentration. Control measurements confirmed that dilution did not alter the position of the RB5 absorption maximum at 622 nm. The suspension was continuously stirred at 300 rpm throughout both dark adsorption and visible-light irradiation. The reactor temperature was maintained at 25 ± 2 °C using a circulating-water jacket to minimize lamp-induced heating. The degradation efficiency of RB5 was monitored using UV–Vis spectrophotometry by measuring the absorbance at 622 nm.

2.8 Photodegradation Kinetics

The photocatalytic decomposition kinetics of RB5 under visible light irradiation were investigated by the Langmuir–Hinshelwood kinetic model. The apparent pseudo-first-order rate constant (k) was determined from the appropriate experimental data according to Eqs. (10) and (11) (Selvinsimpson *et al.* 2021):

$$(-r_i) = -\frac{dC_i}{dt} = \frac{k_s^* K^* C_i}{1+K^* C_i} \quad \ldots (12)$$

$$C_i = C_{i0}{}^* e^{-k^* t} \quad \ldots (13)$$

The Langmuir–Hinshelwood expression is r=kr KC/(1+KC), where kr is the surface-reaction constant and K is the adsorption-equilibrium constant. At relatively low RB5 concentrations, KC≪1, and the equation simplifies to $r=k_{app}C$, where $k_{app}=krK$. Integration gives $\ln(C_0/C_t)=k_{app}t$. Therefore, the pseudo-first-order rate constant used as the optimization response represents the apparent low-concentration form of the Langmuir–Hinshelwood model.

Whereas $_{ks}$ (mol/L/min) denotes the apparent reaction rate constant; k (min^{-1}) indicates the pseudo first order reaction rate of apparent; K (L/mol) represents the adsorption constant; Ci (mol/L) shows the RB5 concentration; Ci0 (mol/L) denotes the starting concentration of RB5 dye; and t (minutes) represents the duration for reaction (Rayya *et al.* 2026).

2.9 Phytotoxicity Tests

The phytotoxicity of the synthesized nanoparticles was evaluated using *Vigna radiata* seeds following the procedure (Kumar and Vaish, 2022). For each treatment, 10 *Vigna radiata* seeds were placed in a Petri dish containing Germitest® paper, with three independent dishes used per treatment (n=30 seeds). Distilled water served as the negative control, while untreated RB5 solution served as the pollutant control. The seeds were exposed to the tested nanoparticle concentrations and incubated at 25 ± 2 °C and 70 ± 5% relative humidity under a 12 h light/12 h dark cycle. Root length was measured using a digital caliper. Results were expressed as mean ± standard deviation and analysed using one-way ANOVA followed by Tukey's test at $p<0.05$.

2.10 Machine-learning Modelling

The 29 BBD observations were used to develop six supervised regression models in MATLAB: Random Forest (RF) (Xiaocui *et al.* 2026), Multilayer Perceptron Artificial Neural Network (MLP-ANN) (Kothari *et al.* 2022). Support Vector Regression (SVR), K-Nearest Neighbours (KNN), Extreme Gradient Boosting (XGBoost), Gaussian Process Regression (GPR).

The four experimental factors were employed as inputs:

$$X = [\text{RB5 concentration, catalyst dosage, pH, W doping }]$$

RB5 removal efficiency and the rate constant were modelled separately as continuous outputs.

Table 2. Machine-learning framework

Component	Description
Inputs	RB5 concentration, catalyst dosage, pH and W doping
Outputs	RB5 removal and rate constant
Models	RF, MLP-ANN, GPR, KNN, XGBoost and SVR
Validation	Leave-one-out cross-validation
Metrics	(R^2), RMSE and MAE
Platform	MATLAB

Scale-dependent models were trained using normalized input data. Model-specific parameters, including tree number, hidden neurons, kernel function, number of neighbours, learning rate, and regularization parameters, were tuned to minimize prediction error.

2.11 Model Validation and Comparison

Leave-one-out cross-validation (LOOCV) was used because the dataset contained 29 observations. In each iteration, one data point was kept for testing, and the remaining 28 observations were used for model training. Hyperparameters were optimized within each training dataset using fivefold internal cross-validation. The examined settings were: RF, 50–500 trees, minimum leaf size 1–4, and 1–4 predictors per split; MLP–ANN, 3–15 hidden neurons and L2 regularization of 10−5–10−2; GPR, squared-exponential, Matérn 3/2, Matérn 5/2, and rational-quadratic kernels; KNN, 2–8 neighbours with Euclidean or city-block distance and uniform or inverse-distance weighting; XGBoost, 50–200 trees, maximum depth 2–4, learning rate 0.01–0.10, and subsampling ratio

0.8–1.0; and SVR, linear, polynomial, and radial-basis kernels, C=0.1–100, and ε=0.001–0.10. Input variables were standardized using the training-set mean and standard deviation. A fixed random seed of 42 was used for reproducibility. This procedure was followed until every data point had been used once as an independent test point.

Predictive performance was evaluated using:

$$R^2 = 1 - \frac{\sum_{i=1}^{n} (y_i - \hat{y}_i)^2}{\sum_{i=1}^{n} (y_i - \bar{y})^2} \quad \ldots (14)$$

$$RMSE = \sqrt{\frac{1}{n}\sum_{i=1}^{n} (y_i - \hat{y}_i)^2} \quad \ldots (15)$$

$$MAE = \frac{1}{n}\sum_{i=1}^{n} |y_i - \hat{y}_i| \quad \ldots (16)$$

where $y_i, \hat{y}_i$, and $\bar{y}$ are the experimental, predicted, and mean experimental values, respectively. The model with the highest cross-validated R^2 and lowest RMSE and MAE was selected for each response. Experimental-versus-predicted and residual plots were used to examine prediction agreement and systematic error. The performance of the best ML model was finally related with the RSM model. In each LOOCV iteration, normalization parameters were calculated using only the 28 training observations. The same training-derived parameters were then applied to the held-out observation, thereby preventing information leakage from the test sample.

3. RESULTS AND DISCUSSION

3.1 Chemical Analysis of Dragon Fruit Peel Extract

Table 3. Major metabolite compounds identified in dragon fruit peel extract by HPLC

Component	Retention Time (min)	Area (%)	Concentration (µg mL⁻¹)
Gallic acid	1.52	24.86	5.12
Catechin	1.91	18.74	3.86
Chlorogenic acid	2.43	12.68	2.61
Caffeic acid	3.08	8.54	1.76
Ferulic acid	3.57	6.92	1.43
Rutin	4.26	9.63	1.98
Quercetin	4.88	7.81	1.61
Kaempferol	5.71	4.52	0.93
Betanin	6.42	3.87	0.80
Phyllocactin	7.36	1.84	0.38
Isorhamnetin	8.24	0.59	0.12

The HPLC analysis of the peel extract confirmed the occurrence of several bioactive phenolic compounds and flavonoids. The abundance of phenolic acids, flavonoids, and betalain pigments demonstrates the promising antioxidant potential of the peel extract. These phytochemicals serve as effective reducing as well as stabilizing agents during the biosynthesis of W-doped $BiVO_4$ nanoparticles by facilitating metal-ion reduction, nanoparticle nucleation, and surface stabilization, thereby promoting the formation of uniform and stable nanostructures.

3.2 Comprehensive Characterization of Synthesized $BiVO_4$ Nanoparticles

Figure 2(a) presents the XRD pattern of the synthesized $BiVO_4$ nanoparticles. The principal reflections at approximately 18.8°, 28.8°, 30.5°, 34.5°, 35.2°, 39.8°, 42.5°, 46.9°, 47.4°, 50.1°, 53.3°, and 58.1° correspond to monoclinic scheelite $BiVO_4$ (JCPDS No. 14-0688). No $Bi_4Ti_3O_{12}$ phase was identified because titanium-containing precursors were not used. The average crystallite size calculated using the Scherrer equation was approximately 27–30 nm. The retention of the monoclinic $BiVO_4$ diffraction pattern after W addition indicates preservation of the primary crystal phase. However, because systematic peak-shift and refined lattice-parameter data were not obtained, XRD alone cannot conclusively demonstrate substitutional W incorporation (Abhale *et al.* 2025).

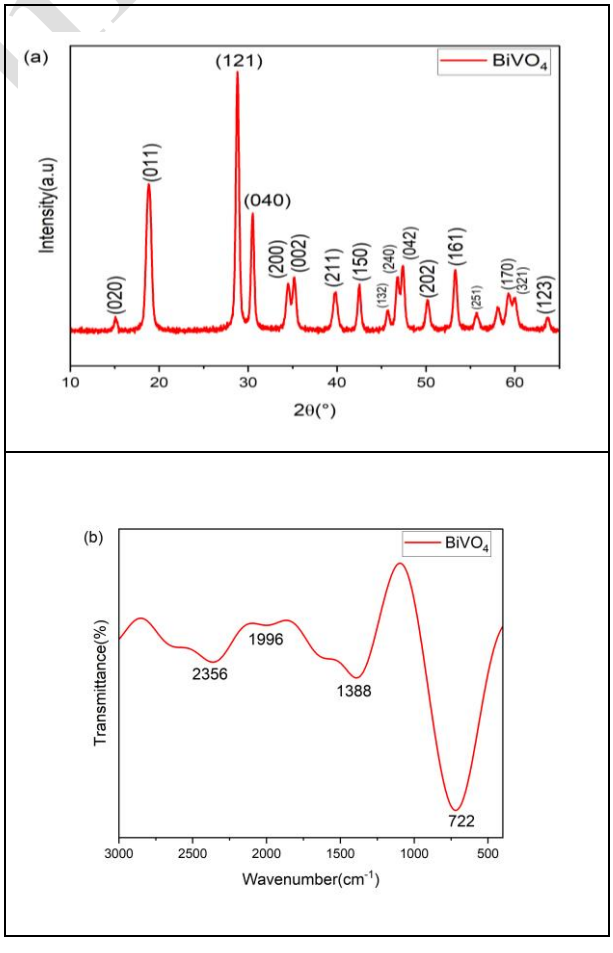

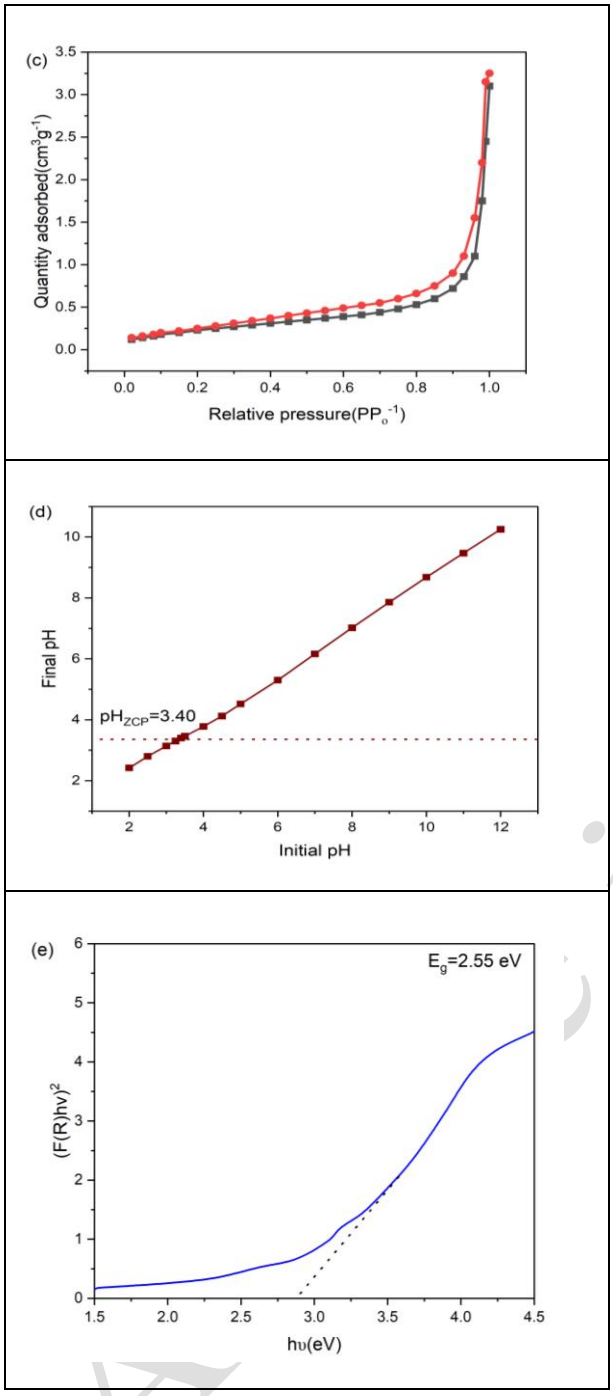

Fig. 2: (a) XRD and (b) FTIR (c) N_2 adsorption/desorption isotherms, (d) zero charge point and (e) Tauc plot generated from the Kubelka-Munk equation of the $BiVO_4$ -NPs

Figure 2(b) presents the FTIR spectrum of the biosynthesized $BiVO_4$ nanoparticles. The broad band within approximately 3000–3200 cm^{-1} is assigned to O–H stretching from surface hydroxyl groups and adsorbed moisture. The weak band at 2356 cm^{-1} is primarily associated with atmospheric CO_2, whereas the feature near 1996 cm^{-1} may arise from weak combination or overtone vibrations and is not assigned to water bending. The band at 1388 cm^{-1} may be associated with residual nitrate or carboxylate-containing phytochemicals. The strong absorption near 722 cm^{-1} is attributed to V–O and Bi–O-related metal–oxygen vibrations, supporting $BiVO_4$ formation.

Figure 2(c) presents the N_2 adsorption–desorption isotherm of the synthesized $BiVO_4$. The observed Type II-like profile with an H4 hysteresis loop suggests particle aggregation and slit-shaped pores. The BET surface area, pore volume, and BJH average pore diameter were 6.8 ± 0.2 m^2 g^{-1}, 0.011 ± 0.001 cm^3 g^{-1}, and 18.6 ± 0.7 nm, respectively. Although the average pore diameter lies within the mesopore range of 2–50 nm, classification as a predominantly mesoporous material should be interpreted cautiously because the isotherm is not a classical Type IV profile.

Figure 2(d) shows the surface-charge characteristics of the synthesized $BiVO_4$ nanoparticles. The measured zeta potential of +3.40 mV indicates a weakly positive surface under the measurement conditions and suggests limited electrostatic colloidal stability. The point of zero charge was approximately $pH_{(ZPC)}$ = 3.40. At pH values below 3.40, protonation produces a net positive surface charge, whereas at pH values above 3.40, deprotonation produces a net negative surface charge. This pH-dependent behaviour can influence RB5 adsorption through electrostatic interactions (Rafaela *et al.* 2022).

The optical band gap of the synthesized $BiVO_4$ nanoparticles was estimated from the Tauc plot obtained using the Kubelka–Munk function (Fig. 2(e)). The calculated band gap energy of 2.55 eV indicates efficient visible-light absorption. Such a narrow band gap facilitates the excitation of electrons from the valence band to the conduction band under solar irradiation, enhancing the generation of electron–hole pairs that drive photocatalytic reactions. These optical characteristics demonstrate the potential of the synthesized $BiVO_4$ nanoparticles for visible-light-assisted photocatalytic applications.

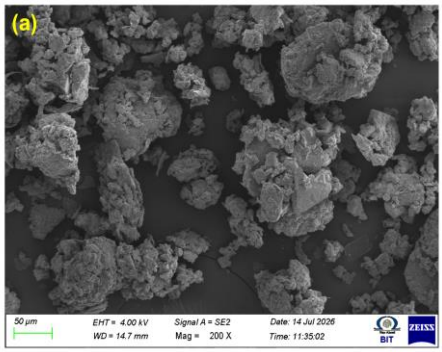

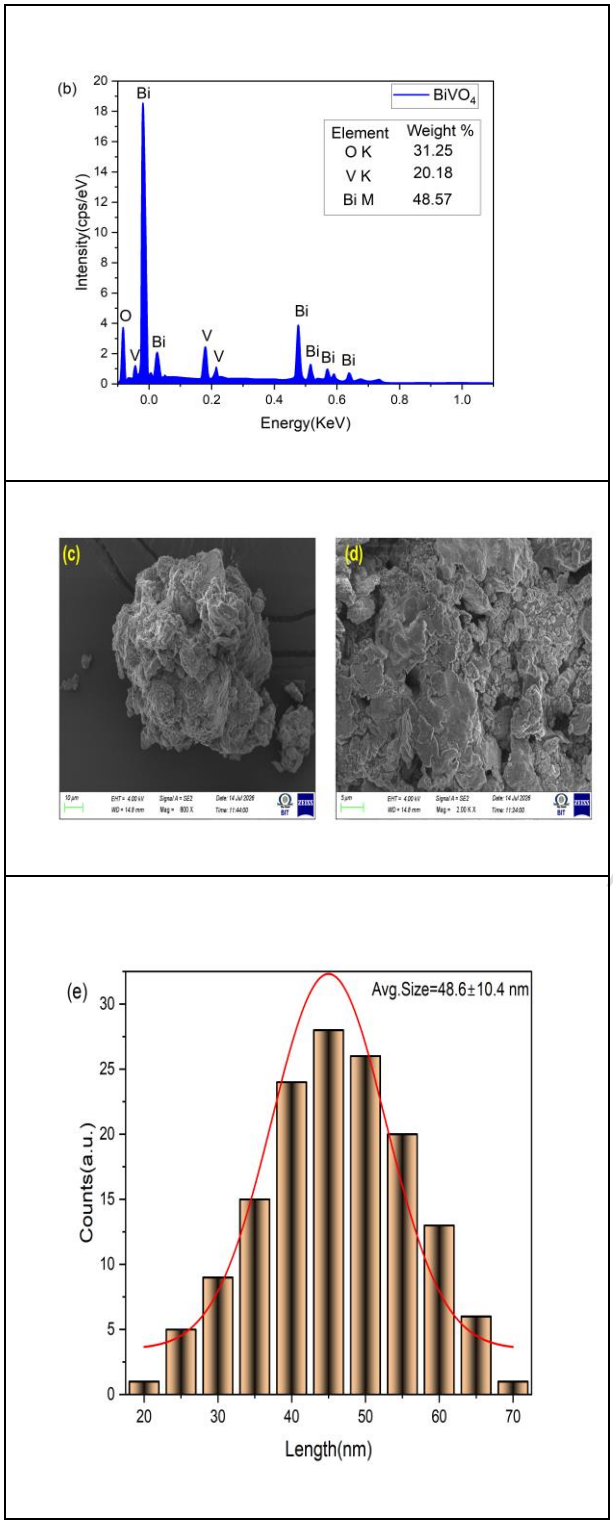

Fig. 3: (a) SEM image at 200x magnification, (b) EDX results, FESEM image at (c) 800x and (d) 2.00 kx magnification and (e) mean particle size of $BiVO_4$ -NPs

In Figure 3(a, c, d and e), synthesized W-doped $BiVO_4$ nanoparticles exhibited predominantly irregular rod-like and ellipsoidal morphologies with a mean particle size of 48.6 ± 10.4nm, which can be attributed to the controlled calcination process. Figure 3(b) presents the EDX spectrum, confirming the presence of Bi, V, O, and W in the analysed sample without detectable foreign elements. EDX confirms the elemental presence of W but does not independently establish its substitutional incorporation into the $BiVO_4$ lattice. The successful synthesis of W-doped $BiVO_4$ nanoparticles was further verified through the combined characterization results. Fig. 4 illustrates the TGA analysis of the synthesized W-doped $BiVO_4$ nanoparticles.

Figure 4 shows substantial multistage mass loss between 25 and 800 °C. The initial loss below approximately 100 °C is attributed to physically adsorbed moisture. The major loss between approximately 100 and 350 °C may be associated with the decomposition of residual phytochemicals, nitrates, and other volatile precursor-derived constituents. The gradual loss above 350 °C may reflect continued removal of residual carbonaceous matter. The subsequent mass loss (approximately 60-65%) corresponds to the removal of residual inorganic species and structural rearrangement associated with Bi–O, V–O, and W–O bonding within the crystal lattice. The relatively low overall weight loss demonstrates the excellent thermal stability of the synthesized monoclinic W-doped $BiVO_4$, indicating its suitability for photocatalytic applications under elevated operating temperatures.

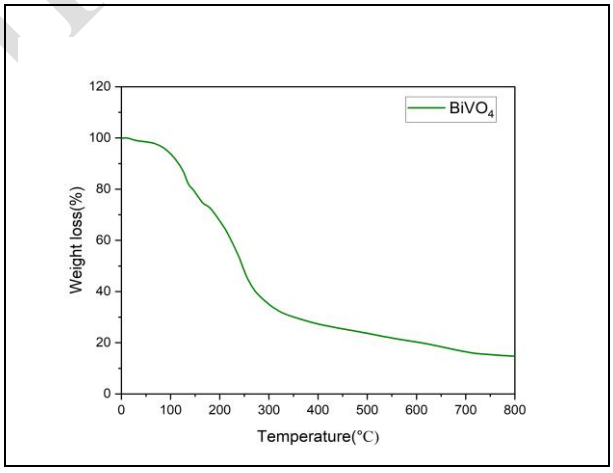

Fig. 4: TGA thermogram of the $BiVO_4$ -NPs

3.3 Experimental Design and Response Values

A four-factor, three-level BBD comprising 29 experimental trials was employed to investigate the effects of initial RB5 concentration (A), W–$BiVO_4$ catalyst dosage (B), initial pH (C), and W-doping level (D). RB5 removal efficiency and apparent pseudo-first-order rate constant were selected as response variables.

Experimental factor combinations and corresponding response values are presented in Table 4. The RB5 removal efficiency varied from 56.20 to 93.40%, whereas the apparent rate constant ranged from

0.00684 to 0.01947 min⁻¹. These variations demonstrate that the investigated operating parameters substantially affected both the extent and rate of RB5 photodegradation.

Table 4. Box–Behnken experimental matrix and response values

Run	RB5 Concentration, (A) (mg L⁻¹)	Catalyst Dosage, (B) (g L⁻¹)	Initial pH, (C)	W Doping, (D) (wt.%)	RB5 Removal (%)	(k) (min⁻¹)
1	40	0.80	9	5	69.60	0.01157
2	40	0.40	6	5	62.20	0.00882
3	20	0.80	9	3	78.90	0.01338
4	40	1.20	3	3	88.80	0.01656
5	20	0.40	6	3	68.50	0.01092
6	40	0.80	6	3	82.40	0.01553
7	20	0.80	3	3	88.10	0.01904
8	40	0.80	6	3	81.70	0.01471
9	40	0.40	9	3	57.20	0.00684
10	60	1.20	6	3	72.60	0.01209
11	40	0.80	6	3	82.20	0.01365
12	60	0.80	6	5	66.50	0.00970
13	60	0.80	6	1	61.40	0.00837
14	40	0.40	6	1	59.80	0.00800
15	40	1.20	9	3	78.80	0.01487
16	20	1.20	6	3	93.40	0.01947
17	40	0.40	3	3	71.30	0.01069
18	40	0.80	6	3	81.90	0.01462
19	20	0.80	6	1	78.60	0.01470
20	40	0.80	3	5	80.60	0.01416
21	40	0.80	3	1	77.30	0.01281
22	60	0.40	6	3	56.20	0.00786
23	60	0.80	3	3	74.70	0.01194
24	40	0.80	6	3	82.00	0.01452
25	40	1.20	6	1	79.50	0.01382
26	40	1.20	6	5	82.70	0.01663
27	60	0.80	9	3	60.20	0.00924
28	20	0.80	6	5	81.40	0.01480
29	40	0.80	9	1	65.40	0.00948

Runs 6, 8, 11, 18, and 24 represent five independently conducted centre-point repetitions at 40 mg L⁻¹ RB5, 0.80 g L⁻¹ catalyst dosage, pH 6, and 3 wt.% W doping. Their mean RB5 removal was 82.04 ± 0.27%, while the mean apparent rate constant was 0.01461 ± 0.00067 min⁻¹. Variation among these runs was used to estimate pure error.

3.4 RSM Model Validation and ANOVA

Quadratic models were developed separately for RB5 removal efficiency and apparent pseudo-first-order rate constant. The ANOVA results for both responses are presented in Table 5. Both quadratic models were statistically significant ($p < 0.0001$). The lack of fit was nonsignificant for RB5 removal ($p = 0.1532$) and the rate constant ($p = 0.6691$) indicating that the residual variation was not significantly greater than the pure experimental error.

For RB5 removal, all four linear terms were significant. In coded variables, the removal model contained linear coefficients of −8.108 for RB5 concentration (A), +10.050 for catalyst dosage (B), −5.892 for pH (C), and +1.750 for W doping (D). Thus, catalyst dosage and W doping exerted positive linear effects, whereas increasing RB5 concentration and pH produced negative effects. For the rate constant, the corresponding coefficients were −0.002759, +0.003359, −0.001652, and +0.000708 min⁻¹. The AB interaction coefficients were −2.125 for removal and −0.001080 min⁻¹ for the rate constant. The AB, AC, AD, and BC

interaction terms were significant, whereas BD and CD were nonsignificant. For the rate constant, the linear terms A, B, C, and D, the interactions AB and AC, and all four quadratic terms were significant. The remaining interaction terms were nonsignificant at the 5% significance level.

Table 5. ANOVA results for the quadratic RSM models

Model Term	Removal F Value	Removal (p) Value	Rate Constant F Value	Rate Constant (p) Value
Model	1166.98	<0.0001	58.23	<0.0001
(A): RB5 concentration	4496.91	<0.0001	246.16	<0.0001
(B): catalyst dosage	6908.50	<0.0001	364.86	<0.0001
(C): initial pH	2374.26	<0.0001	88.21	<0.0001
(D): W doping	209.47	<0.0001	16.22	0.0012
(AB)	102.96	<0.0001	12.57	0.0032
(AC)	40.03	<0.0001	5.90	0.0292
(AD)	7.54	0.0158	1.02	0.3299
(BC)	23.95	0.0002	3.14	0.0980
(BD)	0.912	0.3558	2.67	0.1247
(CD)	1.15	0.3008	0.369	0.5533
(A^2)	599.97	<0.0001	8.26	0.0122
(B^2)	1005.84	<0.0001	29.77	0.0001
(C^2)	275.22	<0.0001	11.29	0.0047
(D^2)	1315.90	<0.0001	54.68	<0.0001
Lack of fit	2.96	0.1532	0.764	0.6691

The model-fit statistics are summarized in Table 6. The removal model achieved predicted $R^2 = 0.9955$ adjusted $R^2 = 0.9983$, and $R^2 = 0.9991$. Differences between adjusted and predicted R^2 values were substantially less than 0.20, demonstrating good agreement.

The corresponding values for the rate-constant model were 0.9831,0.9662 and 0.9271, respectively. The adequate precision values of 120.56 and 29.36 were considerably greater than the minimum desirable value of four, confirming adequate signal-to-noise ratios.

Table 6. Fit statistics of the quadratic RSM models

Response	(R^2)	Adjusted (R^2)	Predicted (R^2)	CV (%)	Adequate Precision	Lack-of-fit (p)
RB5 removal	0.9991	0.9983	0.9955	0.561	120.56	0.1532
Rate constant	0.9831	0.9662	0.9271	4.79	29.36	0.6691

The diagnostic plots showed that the residuals were approximately normally distributed and scattered around zero without an obvious systematic trend. No observation exceeded the Cook's distance limit of one. Furthermore, the Box–Cox analysis recommended no response transformation. These findings confirmed that both quadratic models were suitable for response-surface interpretation and numerical optimization.

3.5 Effects of RB5 Concentration and Catalyst Dosage

Figure 5 presents the combined effects of initial RB5 concentration and W–$BiVO_4$ catalyst dosage on both responses at a fixed initial pH of 6 and W-doping level of 3 wt.%. As shown in Fig. 5a, increasing catalyst dosage enhanced RB5 removal efficiency. A greater catalyst dosage provides more illuminated surface area and a larger number of photocatalytically active sites, thereby increasing the formation of reactive oxygen species.

Conversely, increasing the initial RB5 concentration decreased removal efficiency. At higher dye concentrations, a greater number of RB5 molecules compete for the available active sites. The increased colour intensity of the solution may also restrict light penetration and reduce the number of photons reaching the W–$BiVO_4$ surface.

A similar trend was observed for the apparent rate constant in Fig. 5b. Increasing the catalyst dosage accelerated RB5 degradation, whereas increasing the dye concentration reduced the rate constant. At elevated pollutant loading, the available surface sites and reactive species become insufficient relative to the number of RB5 molecules.

The curvature of both response surfaces demonstrates that the two responses did not vary linearly throughout the design space. The response surfaces also support the significant AB interaction between initial RB5 concentration and catalyst dosage identified by ANOVA. Therefore, a relatively low initial RB5 concentration combined with a high catalyst dosage favoured both greater removal efficiency and faster degradation kinetics.

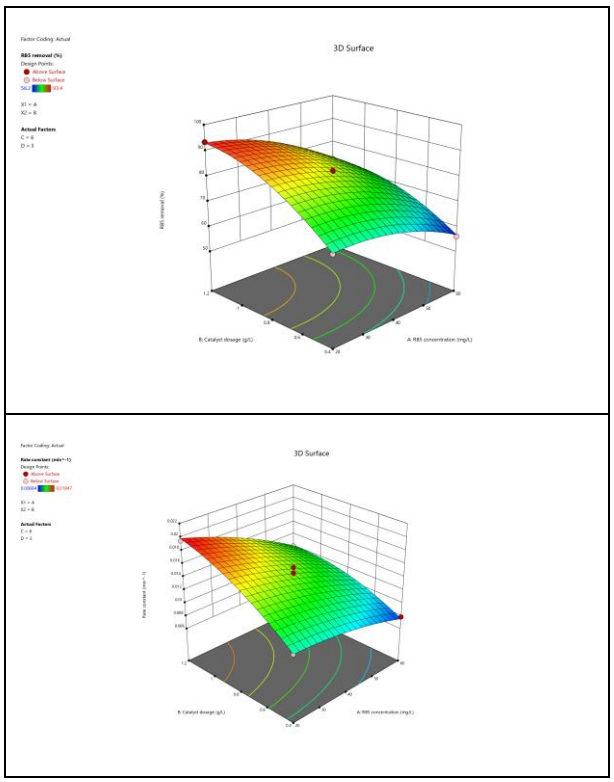

Fig. 5: 3D response surfaces with the combined impact of initial RB5 concentration and W–$BiVO_4$ catalyst dosage on (a) RB5 removal efficiency and (b) apparent pseudo-first-order rate constant at an initial pH of 6 and W-doping level of 3 wt.%

3.6 Multi-response Numerical Optimization

A desirability-function approach was used to determine operating conditions that simultaneously maximized RB5 degradation efficiency and the rate constant while maintaining all four independent variables within their investigated ranges.

The selected solution produced an overall desirability of 1.000 at an initial RB5 concentration of 20.6836 mg L^{-1}, catalyst dosage of 1.16199 g L^{-1}, initial pH of 5.29815, and W-doping level of 3.4384 wt.%. Under these conditions, the models predicted an RB5 removal efficiency of 93.5102% and 0.0200343 min^{-1} constant apparent rate.

The optimum involved a relatively low dye concentration and a high catalyst dosage, producing a favourable ratio of photocatalytically active sites to RB5 molecules. The moderately acidic condition may improve the interaction between RB5 and the W–$BiVO_4$ surface. Meanwhile, the intermediate W-doping level suggests that controlled W incorporation favoured charge-carrier separation. Excessive doping may introduce recombination centres or adversely modify the catalyst surface.

The predicted 0.0200343 min^{-1} rate constant is slightly higher than the maximum experimental value of 0.01947 min^{-1}. It should therefore be reported as a model-predicted value until it is verified through confirmation experiments.

Table 7. Predicted optimum conditions obtained through desirability optimization

Parameter or Response	Optimized Value
Initial RB5 concentration	20.6836 mg L^{-1}
W–$BiVO_4$ catalyst dosage	1.16199 g L^{-1}
Initial pH	5.29815
W-doping level	3.4384 wt.%
Predicted RB5 removal	93.5102%
Predicted rate constant	0.0200343 min^{-1}
Overall desirability	1.000

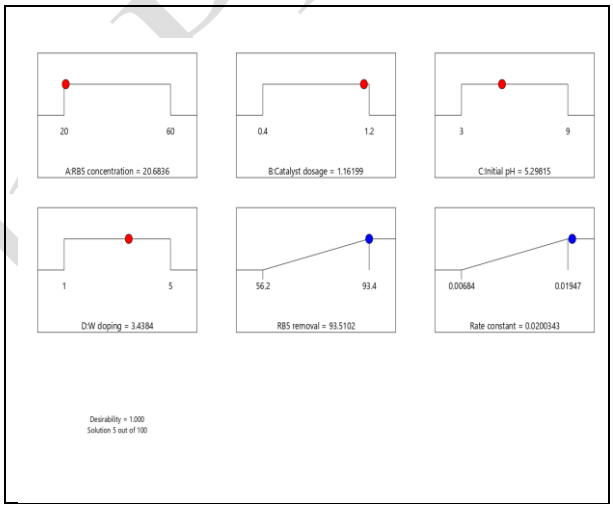

Fig. 6: Desirability ramp showing the simultaneous optimization of initial RB5 concentration, W–$BiVO_4$ catalyst dosage, initial pH, and W-doping level for maximizing RB5 removal efficiency and the pseudo-1st-order apparent rate constant

3.7 Evaluation of Photocatalytic Activity

Pristine $BiVO_4$ served as the undoped reference and achieved 47% RB5 removal after 180 min, with k=0.00295 min^{-1}. In contrast, the maximum experimental BBD response of 93.40% was obtained using W–$BiVO_4$ at 20 mg L^{-1} RB5, 1.20 g L^{-1} catalyst dosage, pH 6, and 3 wt.% W doping. These values represent different catalyst formulations and operating conditions and should not be directly compared without considering these differences. In comparison, iron oxide nanoparticles have been reported to degrade 99.57% of RB5 within 60 min under sunlight, with subsequent pseudo-first-order kinetics and a higher rate constant of

0.065 min^{-1} (R^2 = 0.997), indicating superior photocatalytic performance (Banerjee *et al.* 2025).

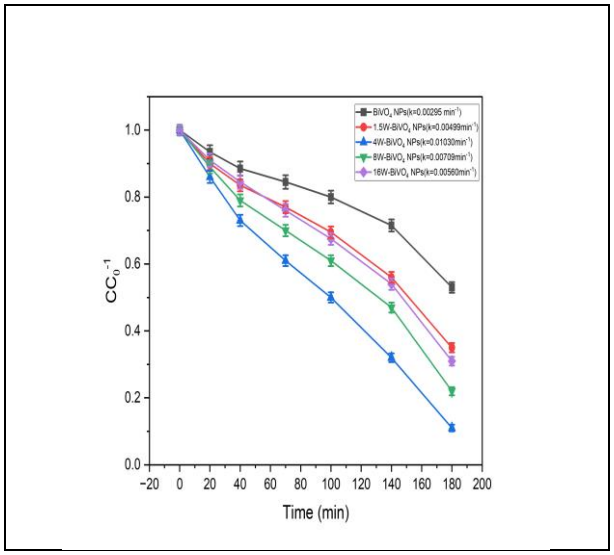

Fig. 7: Photocatalytic degradation profiles of RB5 under visible-light irradiation using pristine $BiVO_4$ and W–$BiVO_4$ containing 1.5, 4, 8, and 16 wt.% nominal W

Reactive Black 5 has a molecular formula of $C_{26}H_{21}N_5Na_4O_{19}S_6$ and a molar mass of approximately 991.82 g mol^{-1}. Its complex aromatic structure, azo linkages, and sulfonate groups can hinder rapid degradation through light-screening, active-site competition, and formation of persistent intermediate products. W doping enhanced RB5 degradation up to an optimum screening level of 4 wt.%, increasing the apparent rate constant from 0.00295 min^{-1} for pristine $BiVO_4$ to 0.01030 min^{-1}. Increasing the W content to 8 and 16 wt.% reduced the rate constant to 0.00709 and 0.00560 min^{-1}, respectively. However, further increasing the W^{6+} content to 8 and 16 wt.% reduced the degradation efficiency, which may be attributed to excessive WO_4 incorporation that decreases the number of available photocatalytically active sites.

3.8 ML Prediction of RB5 Removal Efficiency

Figure 8 compares the experimental and LOOCV-predicted RB5 removal efficiencies obtained using the six ML algorithms. GPR showed the closest agreement with the equality line, achieving R^2_{CV} = 0.991, an RMSE of 0.942%, and an MAE of 0.798%. SVR also demonstrated excellent predictive performance, with R^2_{CV} = 0.979.

XGBoost showed intermediate prediction accuracy, whereas RF, MLP-ANN, and KNN exhibited greater deviations, particularly near the extreme removal values. GPR was therefore identified as the most effective ML model for predicting RB5 removal efficiency within the investigated experimental domain.

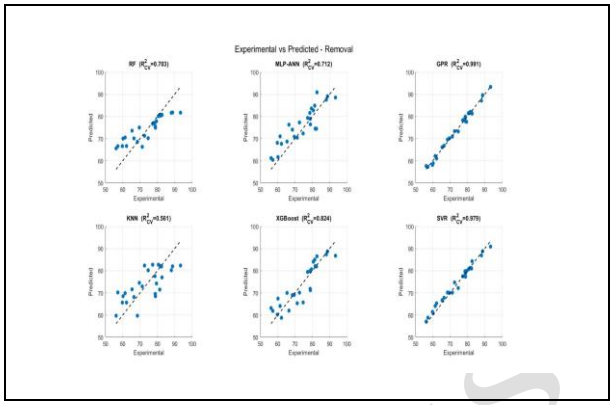

Fig. 8: Experimental versus LOOCV-predicted RB5 removal efficiencies obtained using RF, MLP-ANN, GPR, KNN, XGBoost and SVR

3.9 ML Prediction of the Apparent Rate Constant

The experimental and LOOCV-predicted apparent rate constants are compared in Fig. 9. SVR produced the highest cross-validated coefficient of determination, with R^2_{CV} = 0.924, followed closely by GPR with R^2_{CV}=0.918.

SVR also produced the lowest RMSE of 8.963×10^-4 min^-1. GPR produced a slightly higher RMSE of 9.308×10^-4 min^-1 but provided the lowest MAE of 7.631×10^-4 min^-1. MLP-ANN and XGBoost exhibited intermediate prediction performance. RF and KNN compressed the predictions toward the mean and showed greater errors near the limits of the kinetic-response range.

These findings indicate that SVR provided the most consistent overall prediction of the apparent rate constant based on R^2_{CV} and RMSE, whereas GPR produced the lowest average absolute prediction error.

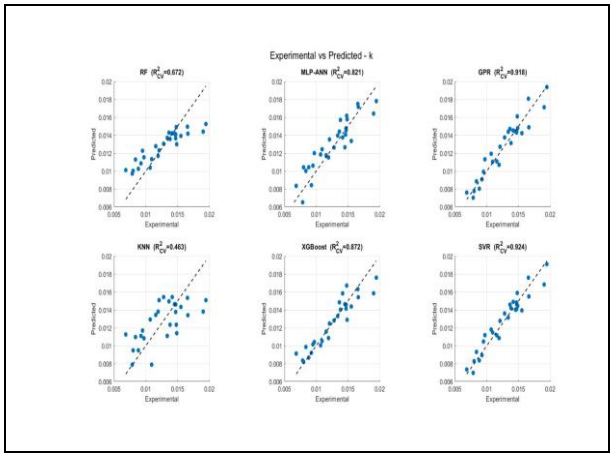

Fig. 9: Experimental versus LOOCV-predicted apparent pseudo-first-order rate constants obtained using RF, MLP-ANN, GPR, KNN, XGBoost and SVR

3.10 Comparative Performance of ML Models

The complete LOOCV performance of six ML models is summarized in Table 8. For the apparent rate constant, SVR produced the maximum R^2_{CV} and the lowest RMSE, whereas GPR provided the minimum MAE. For RB5 removal, GPR produced the maximum R^2_{CV} and the lowest RMSE and MAE. KNN showed the poorest generalization for both responses.

Table 8. LOOCV prediction performance of the investigated ML models

Model	Removal R^2_{CV}	Removal RMSE (%)	Removal MAE (%)	k: R^2_{CV}	k : RMSE (min^{-1})	k : MAE (min^{-1})
RF	0.703	5.421	4.250	0.672	0.001865	0.001403
MLP-ANN	0.712	5.342	4.487	0.821	0.001378	0.001179
GPR	0.991	0.942	0.798	0.918	0.000931	0.000763
KNN	0.561	6.587	5.429	0.463	0.002387	0.001990
XGBoost	0.824	4.175	3.163	0.872	0.001165	0.000832
SVR	0.979	1.444	1.184	0.924	0.000896	0.00077

The corresponding RMSE and MAE comparisons are shown in Fig. 10. The results demonstrate that no single algorithm was uniformly superior for every response and performance metric. Nevertheless, GPR was the preferred model for removal efficiency, while SVR was selected as the best overall predictor of the apparent rate constant.

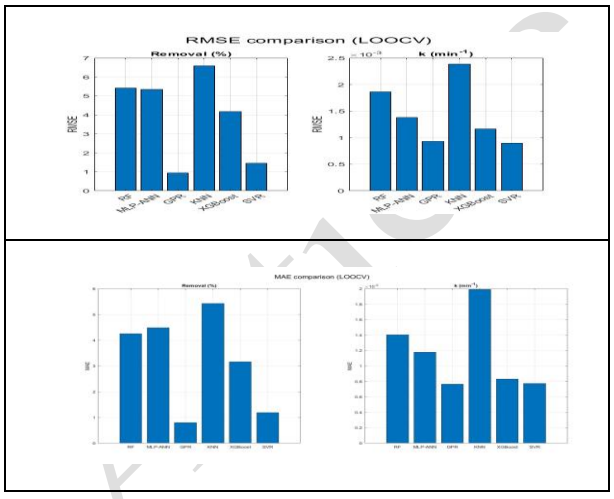

Fig. 10: LOOCV prediction-error comparison of RF, MLP–ANN, GPR, KNN, XGBoost, and SVR: (a) RMSE and (b) MAE for RB5 removal efficiency and the pseudo-1st -order constant apparent rate

The best model was selected primarily using the highest cross-validated R^2 and lowest RMSE, while MAE was used as a complementary measure of average absolute error. Accordingly, GPR was selected for RB5 removal because it produced the highest R^2 (0.991), lowest RMSE (0.942%), and lowest MAE (0.798%). SVR was selected for the rate constant because it produced the highest R^2 (0.924) and lowest RMSE (0.000896 min^{-1}), although GPR produced a marginally lower MAE of 0.000763 min^{-1}.

3.11 Residual Analysis of the ML Predictions

The LOOCV residual distributions for RB5 removal are presented in Fig. 11. GPR produced the narrowest residual range, and its errors were distributed around zero without a pronounced systematic trend. This behaviour supports the superior predictive stability of the GPR model. SVR also produced relatively small residuals.

In contrast, RF, MLP–ANN, KNN, and XGBoost exhibited wider residual distributions and larger deviations at some predicted response levels. The greater residual magnitudes obtained from these models were consistent with their comparatively higher RMSE and MAE values (Rosa *et al.* 2021).

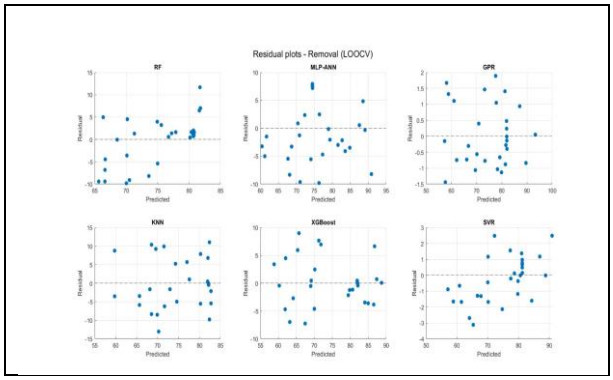

Fig. 11: Residual distributions for LOOCV prediction of RB5 removal efficiency using RF, MLP–ANN, GPR, KNN, XGBoost, and SVR

3.12 Feature-importance Analysis

The feature-importance results obtained from the RF and XGBoost models are shown in Fig. 12. Both tree-based models identified W–$BiVO_4$ catalyst dosage as the most influential predictor of RB5 removal, followed by initial RB5 concentration, initial pH, and W-doping level. This ranking was generally consistent with the RSM results, in which catalyst dosage and initial dye concentration exhibited large F-values. The results indicate that catalyst availability and pollutant loading exerted the strongest predictive influence within the investigated factor ranges. However, feature-importance scores represent the contributions of the variables to model prediction and should not be interpreted as direct mechanistic or causal effects.

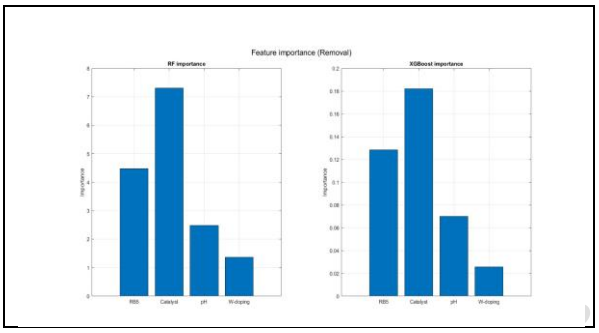

Fig. 12: Relative importance of initial RB5 concentration, W–$BiVO_4$ catalyst dosage, initial pH, and W-doping level for predicting RB5 removal efficiency using (a) RF and (b) XGBoost

RF importance was evaluated using the increase in out-of-bag prediction error after predictor permutation, whereas XGBoost importance was calculated using the normalized gain contributed by splits involving each predictor. Because these metrics are calculated differently, their absolute values should not be directly compared; only the within-model rankings were interpreted.

3.13 Comparison Between RSM and ML Prediction

Figure 13 compares the quadratic RSM removal model with GPR, which was identified as the best ML predictor of RB5 removal. The RSM model achieved a fitted R^2 of 0.9991, whereas GPR achieved a cross-validated R^2_{CV} of 0.9910. Both models therefore represented the RB5 removal response with high accuracy.

RSM provided an interpretable mathematical relationship between the experimental factors and responses. It also enabled the visualization of factor interactions and desirability-based multi-response optimization. In contrast, GPR demonstrated strong out-of-sample predictive capability and successfully captured the nonlinear response pattern using LOOCV.

However, the two coefficients of determination were obtained using different evaluation procedures. The RSM value represents the fit of the quadratic model to the complete experimental dataset, whereas the GPR value represents out-of-sample cross-validated performance. Consequently, the values should not be treated as directly equivalent or used alone to conclude that RSM was superior to GPR. Similarly, the MLP regressor outperformed other machine learning models with R^2 = 0.9676, identifying adsorbent dosage as the most influential parameter (Kumar *et al.* 2026).

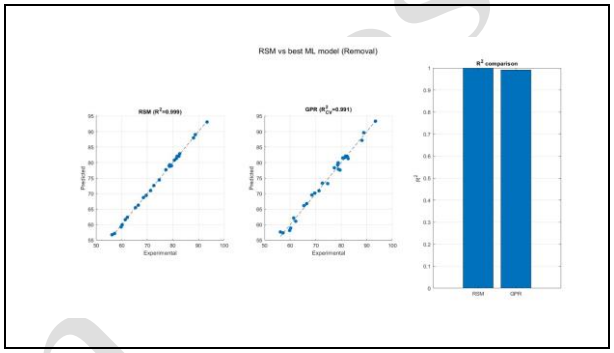

Fig. 13: Comparison of RSM and GPR predictions of RB5 removal efficiency: (a) experimental versus RSM-predicted values, (b) experimental versus GPR LOOCV-predicted values, and (c) comparison of the corresponding coefficients of determination

The RSM R^2 of 0.9991 represents goodness of fit to the complete experimental dataset, whereas the GPR R^2 of 0.991 represents out-of-sample LOOCV prediction. Consequently, these values evaluate different aspects of model performance and are not treated as directly equivalent.

3.14 Evaluation of the Phytotoxicity of $BiVO_4$-NPs and 4W/$BiVO_4$-NPs

The phytotoxicity assessment of $BiVO_4$ nanoparticles ($BiVO_4$-NPs) and 4W/$BiVO_4$ nanoparticles on Vigna radiata seeds was studied after 78 h exposure, as shown in Figure 14(a–b).

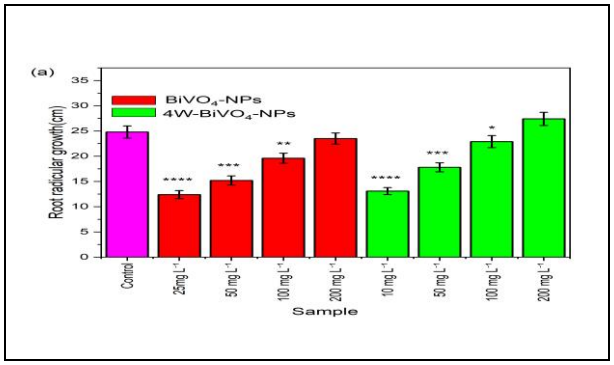

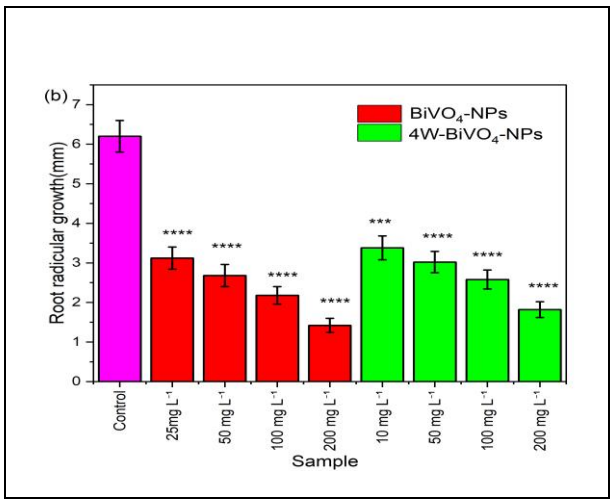

Fig. 14: (a) Root elongation of *Lactuca sativa* and (b) root elongation of Daucus carota after 78 h of exposure to the synthesized nanoparticles

The pristine $BiVO_4$-NPs gradually caused a decrease in root elongation from about 3.1 mm at 25 mg L^{-1} to 1.4 mm at 200 mg L^{-1}, which was about 50–77% inhibition compared to the control. The root elongation values were found to be 3.4, 3.0, 2.6, and 1.8 mm for the 4W/$BiVO_4$-NPs treatment at 25, 50, 100, and 200 mg L^{-1}, respectively, which corresponds to 45–71% phytotoxicity inhibition. The comparatively greater root growth observed for 4W–$BiVO_4$ than for pristine $BiVO_4$ at corresponding concentrations may be associated with W-induced changes in surface chemistry and nanoparticle–seed interactions. However, this interpretation requires supporting surface-characterization and uptake analyses. In summary, even though the concentrations increased, Mg-doped $BiVO_4$ nanoparticles exhibited higher root elongation than the pristine $BiVO_4$ nanoparticles, suggesting their higher environmental compatibility while retaining their potential as green photocatalysts.

4. CONCLUSIONS

This study demonstrated the green synthesis of pristine $BiVO_4$ and W-doped $BiVO_4$ (W–$BiVO_4$) nanocatalysts using dragon-fruit-peel extract for visible-light degradation of Reactive Black 5. The W–$BiVO_4$ nanoparticles exhibited irregular rod-like and ellipsoidal morphologies with a mean particle size of 48.6 ± 10.4 nm. SEM–EDX confirmed the elemental presence of Bi, V, O, and W in the W–$BiVO_4$ sample. Evidence from XRD peak shifts, lattice-parameter variations, and complementary spectroscopic analysis further supported W incorporation into the $BiVO_4$ structure. W addition enhanced RB5 removal from 47% for pristine $BiVO_4$ to 89% for 4W–$BiVO_4$ and increased the apparent pseudo-first-order rate constant from 0.00295 to 0.01030 min^{-1}. Higher W contents of 8 and 16 wt.% reduced the rate constant to 0.00709 and 0.00560 min^{-1}, respectively, demonstrating the importance of controlled W addition.

The effects of initial RB5 concentration, W–$BiVO_4$ dosage, initial pH, and W-doping level were evaluated using a 29-run Box–Behnken design. The quadratic models achieved fitted R^2 values of 0.9991 for RB5 removal and 0.9831 for the apparent rate constant. The maximum experimental performance was 93.40% RB5 removal with an apparent pseudo-first-order rate constant of 0.01947 min^{-1} using 3 wt.% W–$BiVO_4$ at 20 mg L^{-1} RB5, 1.20 g L^{-1} catalyst dosage, and pH 6. Multiresponse optimization predicted 93.51% removal and an apparent rate constant of 0.02003 min^{-1} at 20.68 mg L^{-1} RB5, 1.162 g L^{-1} catalyst dosage, pH 5.30, and 3.44 wt.% W, with a desirability of 1.000. These optimized values remain model-predicted, and experimental confirmation is identified as a valuable future validation step.

Among the six ML algorithms evaluated using LOOCV, GPR provided the best prediction of RB5 removal efficiency with R^2=0.991, whereas SVR provided the best overall prediction of the apparent rate constant with R^2=0.924. The RSM statistics represent fitted model performance, whereas the ML values represent cross-validated predictive performance and are therefore not directly equivalent. Feature-importance analysis identified catalyst dosage and initial RB5 concentration as the dominant predictive variables.

The 78 h phytotoxicity assessment using Vigna radiata at 25–200 mg L^{-1} demonstrated concentration-dependent changes in root growth and provided preliminary toxicity information. Overall, the findings demonstrate the potential of integrating green W–$BiVO_4$ synthesis, RSM optimization, and ML prediction for visible-light treatment of RB5-containing wastewater. Further studies should assess catalyst reusability, post-cycle structural stability, degradation intermediates, total organic carbon removal, mineralization, real-wastewater performance, and comprehensive ecotoxicity before practical implementation.

FUNDING

This research received no specific grant from any funding agency in the public, commercial, or not-for-profit sectors.

CONFLICTS OF INTEREST

The authors declare that there is no conflict of interest.

REFERENCES

Abhale, Y., Patel, K., Paul, R. K., Mishra, S. R., Roy, S., Ahmaruzzaman, M., Ban, T. K., Kumar, D. and Ghotekar, S., Novel bio-inspired fabrication of $BiVO_4$ nanoparticles and their solar light-aided photocatalytic activity for metronidazole antibiotic degradation, *J. Sol-Gel Sci. Technol.*, 115(3), 1580–1597(2025). https://doi.org/10.1007/s10971-025-06872-9

Ameenudeen, S., Unnikrishnan, S. and Ramalingam, K., Statistical optimization for the efficacious degradation of reactive azo dyes using Acinetobacter baumannii JC359, *J. Environ. Manage.*, 279, 111512(2021). https://doi.org/10.1016/j.jenvman.2020.111512

Anishia, S. R. and Rajeswari, S., Green Synthesis and Multifunctional Applications of Moringa Oleifera-enhanced TiO_2 Nanocomposites, *J. Environ. Nanotechnol.*, 14(1), 7–17(2025). https://doi.org/10.13074/jent.2025.03.2511225

Auxilia Ruby, S., Felicita Florence, J. and Asia Thabassoom, H., Green Synthesis of Tungsten Trioxide Nanoparticles Using Selenicereus undatus Peel Extract and their Characterization, *J. Environ. Nanotechnol.*, 14(1), 415–424(2025). https://doi.org/10.13074/jent.2025.03.2441148

Banerjee, S., Mukherjee, A., Dhak, D., Madhogaria, B., Chakraborty, S., Kundu, A. and Dhak, P., Facile biosynthesis of iron oxide nanoparticles from Parthenium hysterophorus extract and investigating their bioactive and photocatalytic applications, *3 Biotech*, 15(12), 422(2025). https://doi.org/10.1007/s13205-025-04581-2

Dash, A., Ragavendran, C. and Rajendran, R., Biogenic Nickel Oxide Nanoparticles: Synthesis, Characterization and Biomedical Potential, *Mol. Biotechnol.*, 68(2), 872–895(2026). https://doi.org/10.1007/s12033-025-01413-9

Hadkar, V. M., Sishu, N. K., Jayabharathi, S. P., Sharmila, A. and Selvaraj, C. I., Biogenic synthesis of Albizia lucidior mediated magnetite nanoparticles (Fe_3O_4 NPs): Therapeutic applications and photocatalytic activity, *Biocatal. Agri. Biotechnol.*, 67, 103676(2025). https://doi.org/10.1016/j.bcab.2025.103676

Kistan, A., Kanchana, V., Mohan, S. and Chitra, M., Green Synthesis of Manganese-Enriched Zinc Oxide Nanoparticles via Dragon Fruit Peel Extracts and their Photocatalytic activity on Methyl Orange, *Res. J. Chem. Environ.*, 29(2), 81–89 (2025). https://doi.org/10.25303/292rjce081089

Kistan, A., Kanchana, V., Mohan, S. and Chitra, M., Innovative Synthesize of ZrO_2 Nanomaterial Using Biodegradable Dragon Fruit Peel Extracts and its Photocatalytic Activity Against Methyl Orange by Uv Radiation, *Rasayan J. Chem.*, 17(1), 199–206 (2024). https://doi.org/10.31788/RJC.2024.1718694

Kistan, A., Mahimairaj, P., Mohan, S., Jeevalatha, R. and Sivakumar, P., Novel Synthesis of S-Doped Zno Nanomaterials Using Selenicereus Undatus Peel Extract for Enhanced UV Photocatalytic Degradation of Methyl Orange, *Rasayan J. Chem.*, 19(1), 575–582 (2026). https://doi.org/10.31788/RJC.2026.1919577

Kothari, M. S., Vegad, K. G., Shah, K. A. and Aly Hassan, A., An artificial neural network combined with response surface methodology approach for modelling and optimization of the electro-coagulation for cationic dye, *Heliyon*, 8(1), e08749(2022). https://doi.org/10.1016/j.heliyon.2022.e08749

Kumar, A., Poornima, S. N., Subbulakshmi, R., Selvaraju, M., G, R. K. and Jayabalan, C., Hierarchical green carbon fibers from banana pseudostem for efficient Pb^{2+} adsorption: Kinetics, isotherms, and machine learning prediction, *Interact.*, 247(1), 188(2026). https://doi.org/10.1007/s10751-026-02534-6

Kumar, M. and Vaish, R., Photocatalytic dye degradation using $BiVO_4$-paint composite coatings, *Mater. Adv.*, 3(14), 5796–5806(2022). https://doi.org/10.1039/d2ma00316c

Kumar, M., Vaish, R., Elqahtani, Z. M., Kebaili, I., Al-Buriahi, M. S., Sung, T. H., Hwang, W. and Kumar, A., Piezo-photocatalytic activity of $Bi_2VO_{5.5}$ for methylene blue dye degradation, *J. Mater. Res. Technol.*, 21, 1998–2012 (2022). https://doi.org/10.1016/j.jmrt.2022.09.130

Liu, Z., Hu, Y., Li, C., Zhang, Z., Shen, T., Zeng, D., Guan, R., Zhou, C. and Dong, P., Fabrication of S-scheme heterojunction consisting of W-doped $BiVO_4$ and biperovskite $Cs_2AgBiBr_6$ for photocatalytic degradation of antibiotics, *J. Colloid and Interf. Sci.*, 696, 137892(2025). https://doi.org/10.1016/j.jcis.2025.137892

Ma, J. S. and Lin, L. Y., Efficient bismuth vanadate homojunction with zinc and tungsten doping via simple successive spin-coating process for photoelectrochemical catalyzing water oxidation, *J. Power Sources*, 499, 229964(2021). https://doi.org/10.1016/j.jpowsour.2021.229964

Pramila, S., Mallikarjunaswamy, C., Nagaraju, G., Kavana, C. P., Chandan, S. and Spoorthy, H. P., Green synthesis of bismuth vanadate nanostructures for efficient photocatalytic and biological studies, *Nano-Struct. Nano-Obj.*, 39, 101198(2024). https://doi.org/10.1016/j.nanoso.2024.101198

Nalina, R., Latha, K. P. and Nagaraju, G., Swift one-pot biosynthesis of copper-bismuth vanadate $Cu_3Bi_4V_2O_{14}$ as a novel photocatalyst using Erythroxylum monogynum seed for efficient visible-light-driven dye degradation, Cr (VI) detoxification, eco-phytotoxic assay and dopamine sensing, *Ceram.*

Int., 52(14), 24212–24233(2026). https://doi.org/10.1016/j.ceramint.2026.03.459

Rafaela, A. A., Casanova, M. F., Frederico, H. L. M. J., Regina, L. T. E. and Andrade, P. C., Photocatalytic oxidation of textile dye using sugarcane bagasse-Nb_2O_5 as a catalyst, *J. Photochem. Photobio. A: Chem.*, 432, 114103 (2022). https://doi.org/10.1016/j.jphotochem.2022.114103

Rayya, N. W., Etefa, K. T., Yimer, A. A., Muleta, G. G. and Beyene, T. T., Green synthesis of Cu-doped ZnO nanocomposites using Phytolacca Dodecandra root extract to improve photocatalytic and antibacterial activity and extend avocado shelf-life, *Sci. Rep.*, 16(1), 2225 (2026). https://doi.org/10.1038/s41598-025-31793-6

Rosa, J. M., Guerhardt, F., Ribeiro Júnior, S. E. R., Belan, P. A., Lima, G. A., Santana, J. C. C., Berssaneti, F. T., Tambourgi, E. B., Vanale, R. M. and Araújo, S. A., Modeling and optimization of reactive cotton dyeing using response surface methodology combined with artificial neural network and particle swarm techniques, *Clean Technol. Environ. Policy*, 23(8), 2357–2367 (2021). https://doi.org/10.1007/s10098-021-02142-8

Sajid, M. M., Assaedi, H. and Zhai, H., Tungsten doping effect on bismuth vanadate (W-doped $BiVO_4$) under visible-light irradiation for photocatalysis, *J. Mater. Sci. Mater. Electron.*, 35(7), 502(2024). https://doi.org/10.1007/s10854-024-12257-5

Salari, M., Nikoo, M. R., Al-Mamun, A., Rakhshandehroo, G. R. and Mooselu, M. G., Optimizing Fenton-like process, homogeneous at neutral pH for ciprofloxacin degradation: Comparing RSM-CCD and ANN-GA, *J. Environ. Manage.*, 317, 115469(2022). https://doi.org/10.1016/j.jenvman.2022.115469

Selvinsimpson, S., Eva Gnana Dhana Rani, S., Ganesh Kumar, A., Rajaram, R., Sharmila Lydia, I. and Chen, Y., Photocatalytic activity of SnO_2/Fe_3O_4 nanocomposites and the toxicity assessment of Vigna radiata, Artemia salina and Danio rerio in the photodegraded solution, *Environ. Res.*, 195, 110787(2021). https://doi.org/10.1016/j.envres.2021.110787

Silva, M. C. R., Castro-Lopes, S., Jerônimo, A. G., Barbosa, R., Lins, A., Trigueiro, P., Viana, B. C., Araujo, F. P., Osajima, J. A. and Peña-Garcia, R. R., Green Synthesis of Er-Doped ZnO Nanoparticles: An Investigation on the Methylene Blue, Eosin, and Ibuprofen Removal by Photodegradation, *Mol.*, 29(2), 391(2024). https://doi.org/10.3390/molecules29020391

Tsay, C. Y., Chung, C. Y., Chen, C. Y., Chang, Y. C., Chang, C. J. and Wu, J. J., Enhanced Photocatalytic Performance of Visible-Light-Driven $BiVO_4$ Nanoparticles through W and Mo Substituting, *Catal.*, 13(3), 475(2023). https://doi.org/10.3390/catal13030475

Xiaocui, W. U., Chen, K., Xue, W., Sun, F., Yang, H. and Cui, Z., From data to catalysis: A hybrid experimental verification-machine learning framework for predicting and enhancing visible-light-driven RhB degradation by template-synthesized g-C_3N_4, *J. Alloys and Compds*, 1052, 186129 (2026). https://doi.org/10.1016/j.jallcom.2026.186129

Xue, Y., Tang, W., Gu, H., Wei, M., Guo, E., Lu, Q. and Pang, Y., Flexible Bi_2MoO_6/N-doped carbon nanofiber membrane enables tetracycline photocatalysis for environmentally safe growth of Vigna radiata, *J. Alloys Compds*, 902, 163860(2022). https://doi.org/10.1016/j.jallcom.2022.163860

Yan, Y., Ni, T., Du, J., Li, L., Fu, S., Li, K. and Zhou, J., Green synthesis of balsam pear-shaped $BiVO_4/BiPO_4$ nanocomposite for degradation of organic dye and antibiotic metronidazole, *Dalton Transac.,* 47, 6089–6101(2018). https://doi.org/10.1039/C8DT00408K

Zaharieva, K., Dimova, S., Ublekov, F. and Penchev, H., Natural Zeolites-Supported Green-Synthesized CeO_2@Polybenzimidazole Hybrid Materials for Dye Degradation, *Eng. Proce.*, 117(1), 24(2026). https://doi.org/10.3390/engproc2025117024

Zhao, G., Ding, J., Zhou, F., Zhao, Q., Wang, K., Chen, X. and Gao, Q., Insight into a novel microwave-assisted W doped $BiVO_4$ self-assembled sphere with rich oxygen vacancies oriented on rGO (W-$BiVO_4$-x/rGO) photocatalyst for efficient contaminants removal, *Separat. Purifi. Technol.*, 277, 119610(2021). https://doi.org/10.1016/j.seppur.2021.119610